Spectral index of synchrotron emission: insights from the diffuse and magnetised interstellar medium

Marco Padovani, Andrea Bracco, Vibor Jelić, Daniele Galli, Elena Bellomi

A&A 651, A116 (2021)
https://doi.org/10.1051/0004-6361/202140799

Astronomy & Astrophysics

Spectral index of synchrotron emission: insights from the diffuse and magnetised interstellar medium

Marco Padovani[1], Andrea Bracco[2], Vibor Jelić[2], Daniele Galli[1], and Elena Bellomi[3]

[1] INAF–Osservatorio Astrofisico di Arcetri, Largo E. Fermi 5, 50125 Firenze, Italy
e-mail: marco.padovani@inaf.it
[2] Ruđer Bošković Institute, Bijenička cesta 54, 10000 Zagreb, Croatia
[3] Observatoire de Paris, LERMA, Sorbonne Université, CNRS, Université PSL, 75005 Paris, France

Received 12 March 2021 / Accepted 20 June 2021

ABSTRACT

Context. The interpretation of Galactic synchrotron observations is complicated by the degeneracy between the strength of the magnetic field perpendicular to the line of sight (LOS), $B_\perp$, and the cosmic-ray electron (CRe) spectrum. Depending on the observing frequency, an energy-independent spectral energy slope s for the CRe spectrum is usually assumed: $s = -2$ at frequencies below $\simeq$400 MHz and $s = -3$ at higher frequencies.
Aims. Motivated by the high angular and spectral resolution of current facilities such as the LOw Frequency ARray (LOFAR) and future telescopes such as the Square Kilometre Array (SKA), we aim to understand the consequences of taking into account the energy-dependent CRe spectral energy slope on the analysis of the spatial variations of the brightness temperature spectral index, β, and on the estimate of the average value of $B_\perp$ along the LOS.
Methods. We illustrate analytically and numerically the impact that different realisations of the CRe spectrum have on the interpretation of the spatial variation of β. We use two snapshots from 3D magnetohydrodynamic simulations as input for the magnetic field, with median magnetic field strength of $\simeq$4 and $\simeq$20 μG, to study the variation of β over a wide range of frequencies ($\simeq$0.1−10 GHz).
Results. We find that the common assumption of an energy-independent s is only valid in special cases. We show that for typical magnetic field strengths of the diffuse ISM ($\simeq$2−20 μG), at frequencies of 0.1−10 GHz, the electrons that are mainly responsible for the synchrotron emission have energies in the range $\simeq$100 MeV−50 GeV. This is the energy range where the spectral slope, s, of CRe varies to the greatest extent. We also show that the polarisation fraction can be much smaller than the maximum value of $\simeq$70% because the orientation of $\mathbf{B}_\perp$ varies across the beam of the telescope and along the LOS. Finally, we present a look-up plot that can be used to estimate the average value of $B_\perp$ along the LOS from a set of values of β measured at different frequencies, for a given CRe spectrum.
Conclusions. In order to interpret the spatial variations of β observed from centimetre to metre wavelengths across the Galaxy, the energy-dependent slope of the Galactic CRe spectrum in the energy range $\simeq$100 MeV−50 GeV must be taken into account.

Key words. cosmic rays – ISM: magnetic fields – ISM: clouds – ISM: structure – radio continuum: ISM – radiation mechanisms: non-thermal

1. Introduction

Studies of diffuse synchrotron emission and its polarisation play a key role in constraining properties of the magnetic fields and of the interstellar medium (ISM) in the Milky Way, especially the cosmic-ray electron (CRe) energy spectrum. They are also relevant for measurements of the cosmic microwave background radiation at high radio frequencies (e.g. Planck Collaboration IV 2020, and references therein) and the cosmological 21 cm radiation from Cosmic Dawn and Epoch of Reionisation (EoR) at low radio frequencies (e.g. Bowman et al. 2018; Gehlot et al. 2019; Mertens et al. 2020; Trott et al. 2020). Galactic synchrotron emission is one of the main foreground contaminants in these cosmological experiments and its emission dominates the radio sky at frequencies below 10 GHz. It is therefore of great importance to obtain a detailed understanding of the spectral and spatial variations of Galactic synchrotron emission in order to successfully mitigate their effects on cosmological observations (for more details see a review by Chapman & Jelić 2019).

The spectrum of Galactic synchrotron emission is usually expressed in terms of the brightness temperature T_ν (defined in Sect. 2.1) which is characterised by a frequency-dependent spectral index $\beta(\nu) = \mathrm{d}\log T_\nu / \mathrm{d}\log\nu$. Spatial variations of β in a given region of the sky reflect spatial variations of the CRe and magnetic field properties in the ISM along the line of sight (LOS) across that region. Full sky maps of Galactic synchrotron emission clearly show spatial variations of β already at the angular resolution of $\simeq$5° (Guzmán et al. 2011). Facilities providing at least three times this angular resolution such as the LOw Frequency ARray, LOFAR (van Haarlem et al. 2013), and in the near future the Square Kilometre Array, SKA (Dewdney et al. 2009), will be able to investigate even finer variations of β.

In terms of frequency, the observed synchrotron spectrum is flatter at low radio frequencies than at high radio frequencies (Roger et al. 1999; Guzmán et al. 2011). Typical values of β estimated from observations at mid and high Galactic latitudes are $-2.59 < \beta < -2.54 \pm 0.01$ between 50 and 100 MHz (Mozdzen et al. 2019) and $-2.62 \pm 0.02 < \beta < -2.60$ between 90 and 190 MHz (Mozdzen et al. 2017), as measured recently by the Experiment to Detect the Global EoR Signature (EDGES). In contrast, in the frequency range 1.4−7.5 GHz, β is -2.81 ± 0.16 (Platania et al. 1998). This difference in the spectral index at low and high radio frequencies is related to aging of the CRe energy spectrum (hereafter simply 'CRe spectrum'), $j_e(E)$.

As CRe propagate through the ISM, they lose energy by a number of energy-loss mechanisms that involve interactions with matter, magnetic fields, and radiation (Longair 2011). These processes deplete the population of relativistic electrons and change their original energy (injection) spectrum. The Galactic CRe spectrum presents many challenges but significant advances have been made in recent years. A number of relevant results have been achieved at high energies (above ≃10 GeV) thanks to detections made by the *Fermi* Large Area Telescope (*Fermi*-LAT; Ackermann et al. 2010), the balloon-borne Pamela experiment (Adriani et al. 2011), and the Alpha Magnetic Spectrometer (AMS-02) on board the International Space Station (Aguilar et al. 2014). Only recently, the two Voyager probes crossed the heliopause, overcoming the problem of solar modulation, and constraining $j_e(E)$ down to $E \simeq 3$ MeV. (Cummings et al. 2016; Stone et al. 2019). Nevertheless, the origin and propagation of CRe are only partly understood because of the degeneracy of a number of parameters and uncertainty about the role of reacceleration, convection, and on the diffusion coefficient (see, e.g. Strong et al. 2007 and Grenier et al. 2015 for comprehensive reviews on this topic).

The uncertainties on the Galactic CRe spectrum limit the interpretation of Galactic synchrotron emission. Depending on the frequency of observation, it is usually assumed that the spectrum of the electrons contributing to the emission can be characterised by a single energy slope. In this paper we show that this assumption results in an oversimplification and needs to be replaced by a more accurate modelling when interpreting observations from centimetre to metre wavelengths. This is especially the case for the recent LOFAR (van Haarlem et al. 2013) polarimetric observations (e.g. Jelić et al. 2015; Van Eck et al. 2017), where observed polarised structures were possibly associated with synchrotron radiation from neutral clouds. As suggested by Van Eck et al. (2017) and further supported by Bracco et al. (2020), the observed polarised synchrotron emission might be originating from low-column-density clouds of interstellar gas along the sight line composed of a mixture of warm and cold neutral hydrogen media, referred to as WNM and CNM, respectively.

In light of these recent results, we partly focus on the effects of the energy-dependent CRe spectral energy slope at a few hundred MHz. However, we also highlight the impact of an energy-dependent energy slope at higher frequencies. This paper is organised as follows. In Sect. 2 we introduce the theory of synchrotron emission and illustrate the effects on the brightness temperature spectral index depending on the parameterisation of the CRe spectrum; in Sect. 3 we apply the above results first to a cloud modelled as a uniform slab, and then to the diffuse, multiphase ISM with the help of 3D magnetohydrodynamic (MHD) simulations, the results of which we then use in Sect. 4 to compute brightness temperature maps, the spectral index, and the polarisation fraction. In Sect. 5 we discuss the effect of the angular resolution of the observations and present a procedure for predicting the average strength of the magnetic field perpendicular to the LOS, $B_\perp$, once the CRe spectrum is set. In Sect. 6 we summarise our main findings.

2. Fundamentals of synchrotron emission

Above ≃10 GeV, the CRe spectrum (i.e. the number of electrons per unit energy, time, area, and solid angle), is approximately a power law in energy, $j_e(E) \propto E^s$. The spectral energy slope (hereafter simply 'spectral slope'), $s(E) = \mathrm{d}\log j_e / \mathrm{d}\log E$, has been measured in the solar neighbourhood by several probes: *Fermi*-LAT established a spectral slope $s = -3.08 \pm 0.05$ in the energy range 7 GeV–1 TeV (Ackermann et al. 2010), the Pamela experiment found $s = -3.18 \pm 0.05$ above the energy region influenced by the solar wind (>30 GeV; Adriani et al. 2011), and AMS-02 determined $s = -3.28 \pm 0.03$ in the energy range 19.0–31.8 GeV and $s = -3.15 \pm 0.04$ in the range 83.4–290 GeV (Aguilar et al. 2014). At low energies, the spectral slope measured by the two Voyager probes in the energy range ≃3–40 MeV is -1.30 ± 0.05 (Cummings et al. 2016; Stone et al. 2019). Thus, at energies below ≃10 GeV, the spectral slope is energy-dependent. As we see below, this has significant consequences for the spectrum of the synchrotron emission observed at frequencies of hundreds of MHz up to tens of GHz.

Generally, models and simulations developed for the interpretation of Galactic synchrotron emission assume that CRe contributing to the emission above and below 408 MHz have $s = -3$ and $s = -2$, respectively (see, e.g. Sun et al. 2008; Waelkens et al. 2009; Reissl et al. 2019; Wang et al. 2020). This simplification is usually made to avoid time-consuming calculations, and is based on observations supporting a flatter spectrum below 408 MHz (see, e.g. Reich & Reich 1988a,b; Roger et al. 1999). In Sect. 2.2 we show that this assumption turns out to be inaccurate at both low and high frequencies, leading to misinterpretation of the synchrotron observations, in particular of the spatial variations of the spectral index β. To support this claim, we consider the two realisations of the local CRe spectrum by Orlando (2018) and Padovani et al. (2018) shown in Fig. 1. The former is based on multifrequency observations, from radio to γ rays, and Voyager 1 measurements through propagation models, and is representative of intermediate Galactic latitudes ($10° < |b| < 20°$) that include most of the local radio synchrotron emission within a radius of ∼1 kpc around the Sun; the latter is given by an analytical four-parameter fitting formula that perfectly reproduces the power-law behaviour measured at low and high energies (see also Ivlev et al. 2015). As shown by the inset in Fig. 1, the spectra by Orlando (2018) and that of Padovani et al. (2018) differ by less than ∼25% over the range of energies of interest here, below $E \simeq 50$ GeV. As we see in Sect. 3.1, synchrotron observations can also constrain these two parameterisations.

CRe at a given energy emit over a broad range of frequencies and, conversely, the synchrotron emission observed at a given frequency comes from a broad range of CRe energies. Before focusing on the frequency range of LOFAR observations (115–189 MHz; see Sect. 4), we consider frequency ranges characteristic of all-sky Galactic radio surveys both at low (45–408 MHz; Guzmán et al. 2011) and high frequencies (1–10 GHz; Platania et al. 1998). For $B_\perp \simeq 2$ to 20 μG, as expected in the diffuse ISM (e.g. Heiles & Troland 2005; Beck 2015; Ferrière 2020), CRe that account for nearly all of the observed synchrotron emission have energies ranging from ≃100 MeV to 50 GeV (see Sect. 2.2)[1]. In this energy range, the spectral slope s shows large variation with energy: between −1.8 and −3.3 and between −1.5 and −3.2, for the spectra modelled by Orlando (2018) and Padovani et al. (2018), respectively (see Fig. 2).

[1] We note that CRe in the energy range 100 MeV–50 GeV are affected by energy losses such as bremsstrahlung only after crossing column densities $\gtrsim 10^{25}$ cm^{-2} (see, e.g. Padovani et al. 2009, 2018), much larger than those typical of the diffuse medium. Therefore, we compute synchrotron emissivities without accounting for any attenuation of the CRe spectrum.

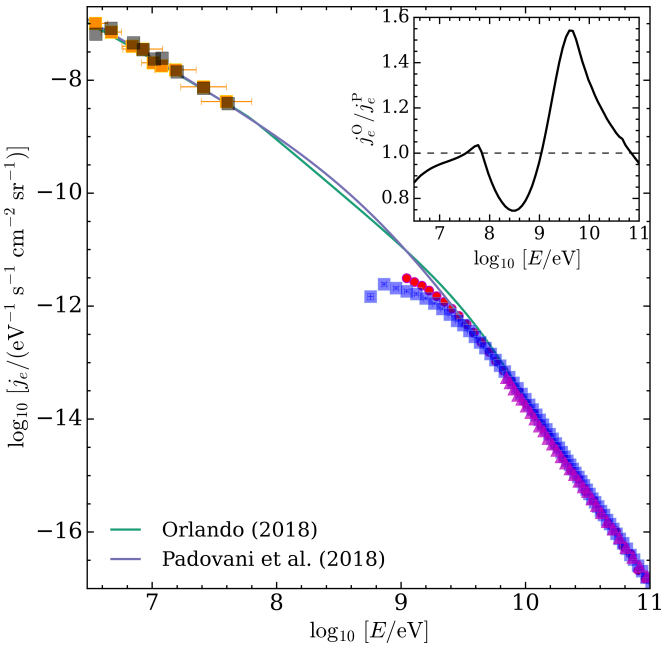

Fig. 1. CRe spectrum according to Orlando (2018; green line) and Padovani et al. (2018; violet line). The inset shows the ratio of the spectra (O = Orlando, P = Padovani; solid black line). Data: Voyager 1 (orange squares; Cummings et al. 2016); Voyager 2 (grey squares; Stone et al. 2019); *Fermi*-LAT (magenta triangles; Ackermann et al. 2010); Pamela (red circles; Adriani et al. 2011); AMS-02 (blue squares; Aguilar et al. 2014).

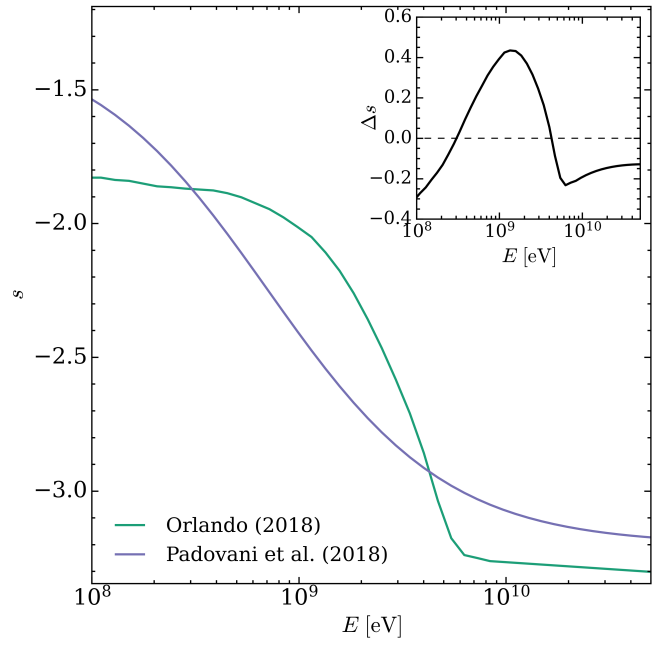

Fig. 2. Spectral slope vs. energy of the CRe spectra by Orlando (2018; green line) and Padovani et al. (2018; violet line) in the energy range relevant for our study (100 MeV−50 GeV). The inset shows the difference Δs between the spectral slope of the two spectra.

2.1. Basic equations

Here we summarise the basic equations for the calculation of the synchrotron brightness temperature, T_ν (see, e.g. Ginzburg & Syrovatskii 1965, for details). At any given position $\mathbf{r}$ in a cloud, the specific emissivity[2] can be split into two components linearly polarised along and across the component of the magnetic field perpendicular to the LOS, $\mathbf{B}_\perp(\mathbf{r})$,

$$\varepsilon_{\nu,\parallel}(\mathbf{r}) = \int_{m_e c^2}^{\infty} \frac{j_e(E)}{v_e(E)} P^{\mathrm{em}}_{\nu,\parallel}(E,\mathbf{r})\,\mathrm{d}E, \quad (1)$$

$$\varepsilon_{\nu,\perp}(\mathbf{r}) = \int_{m_e c^2}^{\infty} \frac{j_e(E)}{v_e(E)} P^{\mathrm{em}}_{\nu,\perp}(E,\mathbf{r})\,\mathrm{d}E\,,$$

where

$$P^{\mathrm{em}}_{\nu,\parallel}(E,\mathbf{r}) = \frac{\sqrt{3}e^3}{2m_e c^2} B_\perp(\mathbf{r})[F(x)-G(x)], \quad (2)$$

$$P^{\mathrm{em}}_{\nu,\perp}(E,\mathbf{r}) = \frac{\sqrt{3}e^3}{2m_e c^2} B_\perp(\mathbf{r})[F(x)+G(x)]$$

are the power per unit frequency emitted by an electron of energy E at frequency ν for the two polarisations. Here, $B_\perp = |\mathbf{B}_\perp|$, v_e is the electron velocity, $x = \nu/\nu_c$, and ν_c is the critical frequency given by

$$\nu_c[B_\perp(\mathbf{r}), E] = \frac{3eB_\perp(\mathbf{r})}{4\pi m_e c}\left(\frac{E}{m_e c^2}\right)^2. \quad (3)$$

The functions $F(x)$ and $G(x)$ are defined by

$$F(x) = x\int_x^\infty K_{5/3}(\xi)\mathrm{d}\xi, \quad (4)$$

and

$$G(x) = xK_{2/3}(x)\,, \quad (5)$$

where $K_{5/3}$ and $K_{2/3}$ are the modified Bessel functions of order 5/3 and 2/3, respectively. The corresponding Stokes Q_ν and U_ν specific emissivities are

$$\varepsilon_{\nu,Q}(\mathbf{r}) = [\varepsilon_{\nu,\perp}(\mathbf{r}) - \varepsilon_{\nu,\parallel}(\mathbf{r})]\cos[2\varphi(\mathbf{r})] \quad (6)$$

and

$$\varepsilon_{\nu,U}(\mathbf{r}) = [\varepsilon_{\nu,\perp}(\mathbf{r}) - \varepsilon_{\nu,\parallel}(\mathbf{r})]\sin[2\varphi(\mathbf{r})]\,, \quad (7)$$

where $\varphi(\mathbf{r})$ is the local polarisation angle counted positively clockwise. The orientation of $\mathbf{B}_\perp$ rotated by $\pm 90°$ gives the local polarisation angle (modulo 180°). The emissivities are integrated along the LOS to obtain the specific intensity (brightness) for each polarisation, $I_{\nu,\parallel}$ and $I_{\nu,\perp}$, and the Stokes parameters Q_ν and U_ν. We also compute the polarisation fraction

$$p = \frac{P_\nu}{I_\nu} = \frac{\sqrt{Q_\nu^2 + U_\nu^2}}{I_\nu}\,, \quad (8)$$

where $I_\nu = I_{\nu,\parallel} + I_{\nu,\perp}$. Finally, the flux density, S_ν, obtained from the convolution of the specific intensity integrated along the LOS with the telescope beam is converted into brightness temperature by the relation

$$T_\nu = 10^{-23}\frac{S_\nu c^2}{2k_{\mathrm{B}}\Omega\nu^2}\ \mathrm{K}\,, \quad (9)$$

where $\Omega = \pi\theta_b^2/(4\ln 2)$, θ_b is the full width of the beam at half its maximum intensity, and k_{B} is the Boltzmann constant. Here, S_ν is in Jy beam^{-1} and the other quantities are in cgs units. If the CRe spectrum is a single power law, $j_e(E) \propto E^{-s}$, then $S_\nu \propto \nu^\alpha$, with $\alpha = (s+1)/2$, and $T_\nu \propto \nu^\beta$, with $\beta = (s-3)/2$ (Ginzburg & Syrovatskii 1965).

[2] The specific emissivity has units of power per unit volume, frequency, and solid angle.

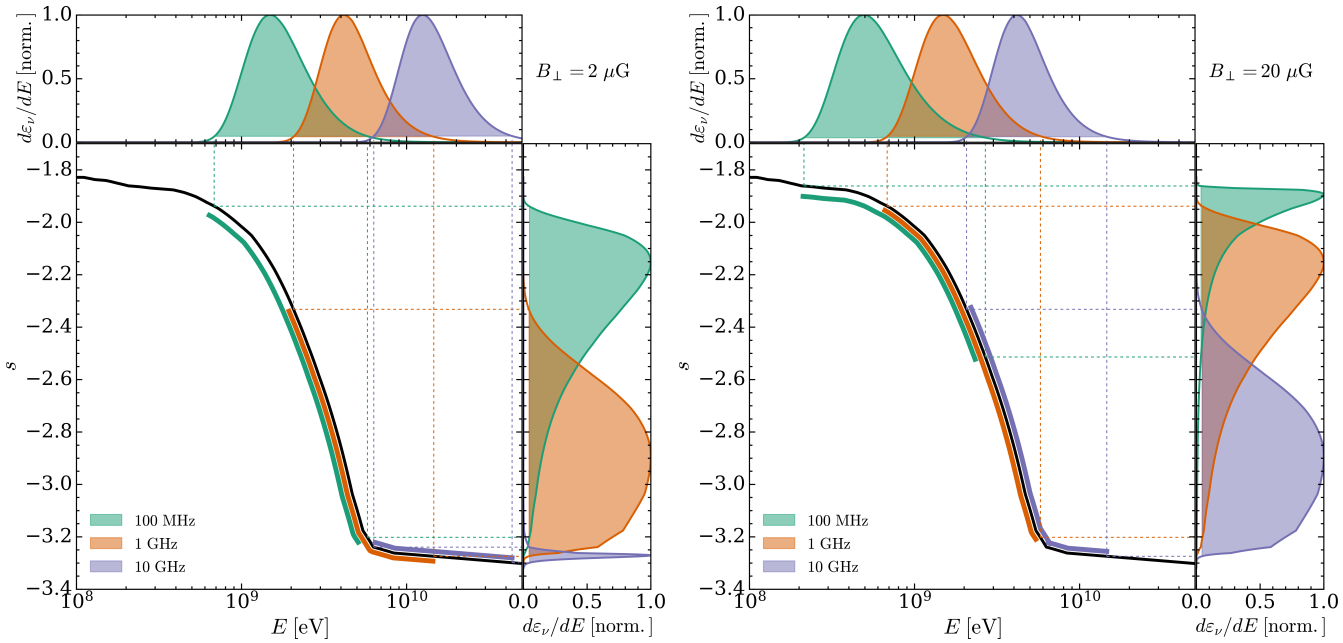

Fig. 3. *Left panel*, *upper plot*: integrand of the specific emissivity, $\mathrm{d}\varepsilon_\nu/\mathrm{d}E$, as a function of the energy E, normalised to its maximum value and summed over the two polarisations (Eqs. (1)), computed at 100 MHz, 1 GHz, and 10 GHz (green, orange, and violet line, respectively), for $B_\perp = 2$ μG. The coloured area below each curve corresponds to 95% of the total emissivity. *Right plot*: Same as the upper plot, as a function of the CRe spectral slope s. *Main plot*: Spectral slope as a function of the energy for the CRe spectrum by Orlando (2018; black solid line). Coloured lines show the range of energies (and the corresponding spectral slopes) contributing to 95% of the specific emissivity. *Right panel*: same as *left panel*, but for $B_\perp = 20$ μG.

2.2. Contributions to synchrotron emission from 100 MHz to 10 GHz

In Sect. 2 we mention that the assumption of an energy-independent slope s can introduce severe biases in the reliability of models and numerical simulations and ultimately affect the interpretation of synchrotron observations, such as the spatial variation of β. To prove this, we consider three observing frequencies (100 MHz, 1 GHz, and 10 GHz) representative of all-sky Galactic radio surveys (Platania et al. 1998; Guzmán et al. 2011) and two extreme values for $B_\perp$ (2 and 20 μG) consistent with the magnetic field strength expected in the diffuse medium (Heiles & Troland 2005; Beck 2015; Ferrière 2020). To identify the range of energies contributing to the specific emissivity for a given value of ν and $B_\perp$, we examine the integrands $\mathrm{d}\varepsilon_\nu/\mathrm{d}E$ summed over the two polarisations (Eqs. (1)). As shown in the upper panels of Fig. 3, $\mathrm{d}\varepsilon_\nu/\mathrm{d}E$ has a well-defined maximum. For each frequency, we compute the energy range around the energy of the maximum, where the specific emissivity is equal to 95% of its total. This fiducial 95% level is meant to show that most of the synchrotron emission at a given frequency originates from a definite, albeit broad, energy range of CRe. The resulting energy ranges (and the corresponding ranges of spectral slope s derived for the CRe spectrum by Orlando 2018) are listed in Table 1. Looking at the ranges of s at each frequency, it is clear that only in the extreme case of high frequencies ($\nu \gtrsim 10$ GHz) and very small $B_\perp$ ($\simeq$2 μG) is the hypothesis of an energy-independent spectral slope accurate (in this case $s \simeq -3.3$). We note that the energy and the spectral slope intervals are the same for a given $\nu/B_\perp$ ratio. This is because the total power per unit frequency, P_ν^{em}, emitted at a frequency ν by an electron of energy E in a field $B_\perp$, peaks at an energy proportional to $\sqrt{\nu/B_\perp}$ (see, e.g. Longair 2011). Figure 3 shows that, for the typical frequency range of synchrotron observation in the diffuse ISM and for the expected values of $B_\perp$, CRe with energies between 100 MeV and 50 GeV are responsible for almost all the non-thermal emission. In this energy range, the spectral slope has the largest variation, and so the assumption of an energy-independent s is not correct.

Table 1. Ranges of energy E and spectral slope s for two values of $B_\perp$ and for a set of frequencies.

ν [GHz]	$B_\perp = 2$ μG		$B_\perp = 20$ μG	
	E [GeV]	s	E [GeV]	s
0.1	[0.7,5.8]	[−3.20, −1.94]	[0.2,2.7]	[−2.52, −1.86]
1	[2.1,14.6]	[−3.27, −2.33]	[0.7,5.8]	[−3.20, −1.94]
10	[6.3,43.6]	[−3.30, −3.24]	[2.1,14.6]	[−3.27, −2.33]

Notes. The ranges of E and s have been derived for the CRe spectrum by Orlando (2018) by integrating $\mathrm{d}\varepsilon_\nu/\mathrm{d}E$ in an energy range around the peak value until 95% of the total specific emissivity is recovered.

For the sake of simplicity, we have only considered the case of the CRe spectrum by Orlando (2018). Using that of Padovani et al. (2018) instead, the energy intervals we obtain are similar, as the two spectra differ on average by 25% (see Sect. 2 and Fig. 1). However, the spectral slope intervals change (see Fig. 2). This means that the use of a particular CRe spectrum has a major influence on the interpretation of the observations. In the following section we show how observational estimates of the brightness temperature spectral index help to constrain the accuracy of a CRe spectrum.

3. Modelling synchrotron emission

In this section we first consider a cloud modelled as a simple uniform slab to show how specific realisations of the CRe spectrum

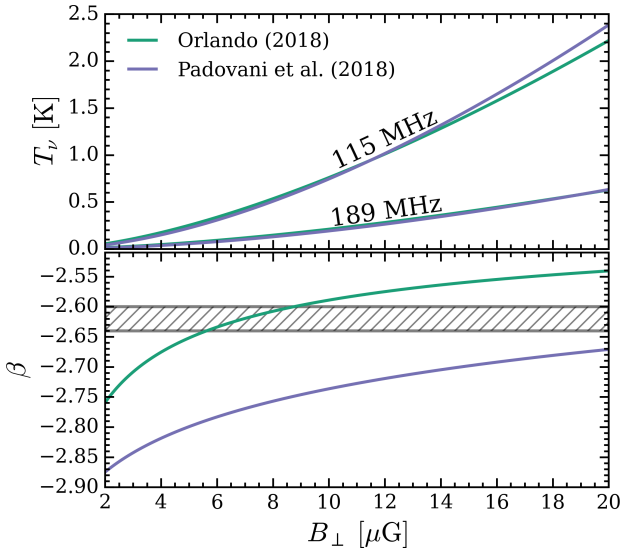

Fig. 4. *Upper panel*: brightness temperature T_ν as a function of $B_\perp$ computed at $\nu = 115$ and 189 MHz with the CRe spectra by Orlando (2018; green line) and Padovani et al. (2018; violet line) for a slab of thickness 1 pc, with an angular resolution $\theta_b = 4'$. *Lower panel*: brightness temperature spectral index β as a function of $B_\perp$ (same colour coding as in the *upper panel*). The hatched region highlights typical values of β at intermediate and high latitudes (Mozdzen et al. 2017).

can be ruled out by comparison with observational estimates of β (Sect. 3.1). We then describe the numerical simulations that we use in the rest of the paper to study the spatial variations of β and of the polarisation fraction (Sect. 3.2).

3.1. Uniform slab

To show the importance of an accurate modelling of the CRe spectrum, we compute the brightness temperature, T_ν, for a slab with a fixed, spatially uniform component of the magnetic field $B_\perp$, varying from 2 to 20 μG as specified in Sect. 2, exposed to a flux of CRe, $j_e(E)$, given by the Orlando (2018) and Padovani et al. (2018) spectra. For illustration, we select the frequency range $\nu = 115$–189 MHz, with a frequency resolution of 183 kHz and assume an angular resolution of $\theta_b = 4'$. These parameters are representative of the LOFAR High Band Antenna observations carried out by Jelić et al. (2015). We assume a thickness of the slab of 1 pc, although the brightness temperature can be easily scaled for any value. We then compute the spectral index, β, through a linear fit of $\log T_\nu$ versus $\log \nu$ for each $B_\perp$ value.

The brightness temperatures generated by the two realisations of the CRe spectrum are on average within ≃25% of each other (upper panel of Fig. 4), of the order of a few to several K. Assuming a synchrotron polarisation fraction of $p \approx 70\%$ (more details in Sect. 4.3), the polarised intensity would be of the same order as T_ν. This is exactly the amount of diffuse polarised emission observed by LOFAR in the range 100–200 MHz (e.g. Jelić et al. 2014, 2015; Van Eck et al. 2017). These simple arguments support the scenario suggested by Van Eck et al. (2017) and Bracco et al. (2020) where parsec-scale neutral clouds in the diffuse ISM could significantly contribute to the Faraday-rotated synchrotron polarisation observed with LOFAR. However, if we compare the value of β (lower panel of Fig. 4) with typical values derived from observations at intermediate and high Galactic latitudes (Mozdzen et al. 2017, shaded strip in the lower panel of Fig. 4), it is evident that in this example only the spectrum by Orlando (2018) is consistent with the observations, and only for values of $B_\perp$ of the order of 6–9 μG, while the one by Padovani et al. (2018) requires unrealistically high values of $B_\perp$. As this example illustrates, the constraint imposed by the highly accurate determination of the spectral index β allowed by current instruments is a strong motivation to further and thoroughly model the total and polarised synchrotron emission of the diffuse ISM.

3.2. Numerical simulations

We now compute synthetic observations of synchrotron emission adopting state-of-the-art numerical simulations of the diffuse, magnetised, multiphase, turbulent, and neutral atomic ISM. Our approach here is not to consider the simulations described below as true representations of any given LOS in the diffuse ISM, but rather as a laboratory with which to study realistic physical conditions of the multiphase medium where synchrotron emission may originate. In particular, we perform numerical simulations of the diffuse ISM using the RAMSES code (Teyssier 2002; Fromang et al. 2006), a grid-based solver with adaptive mesh refinement (Berger & Oliger 1984), and a fully treated tree data structure (Khokhlov 1998).

The gas density of the medium we consider is typically dominated by neutral hydrogen that can be traced via the 21 cm emission line (Heiles & Troland 2003a,b; Murray et al. 2015, 2018). This line is usually decomposed into several Gaussian components (Kalberla & Haud 2018; Marchal et al. 2019) associated to distinct gas phases in pressure balance: a dense cold neutral medium, CNM, with temperature and density $T \simeq 50$ K and $n_H \simeq 50$ cm^{-3}, respectively, immersed in a diffuse warm neutral medium, WNM, with $T \simeq 8000$ K and $n_H \simeq 0.3$ cm^{-3}, and a third intermediate unstable phase, with temperature comprised between those of the CNM and the WNM (e.g. Wolfire et al. 2003; Bracco et al. 2020). Field (1965) and Field et al. (1969) pointed out that the microphysical processes of heating and cooling naturally lead to two thermally stable phases (CNM and WNM) and one thermally unstable phase coexisting in a range of thermal pressure. Through the thermal processes of condensation and evaporation, and with the help of turbulent transport and turbulent mixing, the diffuse matter can flow from one stable state to the other.

The local diffuse matter in our Galaxy is simulated over a box of 50 pc with periodic boundary conditions, using a fixed grid of 128^3 pixels, corresponding to an effective resolution of 0.39 pc. The initial state is characterised by a homogeneous density $n_H = 1.5$ cm^{-3}, a temperature $T = 8000$ K, and a uniform magnetic field $\boldsymbol{B}_0 = B_0 \hat{e}_x$. We consider two snapshots of the simulation, one with a standard average magnetic field strength, $B_0 = 4$ μG (hereafter, the 'weak field' case), and one with a stronger $B_0 = 20$ μG (hereafter, the 'strong field' case). The gas evolves under the joint influence of turbulence, magnetic field, radiation field, and thermal instability, and separates in three different phases: CNM, WNM, and unstable. A turbulent forcing is applied to mimic the injection of mechanical energy into the diffuse ISM. Following Schmidt et al. (2009) and Federrath et al. (2010), this forcing, modelled by an acceleration term in the momentum equation, is driven through a pseudo-spectral method. The turbulent acceleration parameter is set to 2.77×10^{-3} kpc Myr^{-2}. Using classical notation, the dimensionless compressible parameter for the turbulent forcing modes, ζ_0, ranges from pure solenoidal modes ($\zeta_0 = 1$) to pure compressible modes ($\zeta_0 = 0$). We set $\zeta_0 = 0.5$.

The matter is assumed to be illuminated on all sides by an isotropic spectrum of UV photons set to the standard interstellar

Table 2. Minimum and maximum values of the strength of the magnetic field in the plane perpendicular to the LOS i, $B_{jk} = (B_j^2 + B_k^2)^{1/2}$, and its median value $\tilde{B}_{jk}$ for the two cases of weak and strong field.

	LOS$_i$	B_{jk} [μG]	$\tilde{B}_{jk}$ [μG]
Weak field ($B_0 = 4$ μG)	x	$[1.1 \times 10^{-3}, 12]$	$2.02^{+0.88}_{-0.75}$
	y	$[1.5 \times 10^{-3}, 16]$	$4.26^{+0.73}_{-0.71}$
	z	$[9.8 \times 10^{-3}, 13]$	$4.22^{+0.71}_{-0.74}$
Strong field ($B_0 = 20$ μG)	x	$[3.6 \times 10^{-4}, 6]$	$0.80^{+0.38}_{-0.30}$
	y	$[17, 22]$	$19.19^{+0.33}_{-0.41}$
	z	$[17, 22]$	$19.19^{+0.33}_{-0.40}$

Notes. Errors on $\tilde{B}_{jk}$ are estimated using the first and third quartiles. Subscripts i, j, and k follow the cyclic permutation of Cartesian coordinates $(ijk) = \{xyz, yzx, zxy\}$.

radiation field (Habing 1968). To correctly describe the thermal state of the diffuse ISM, we have included the heating induced by the photoelectric effect on interstellar dust grains and secondary electrons produced during cosmic-ray propagation, and the cooling induced by emission of Lyman-α photons, the fine-structure lines of OI and CII, and the recombination of electrons onto grains. All these processes, described in Appendix B of Bellomi et al. (2020), are modelled with the analytical formulae given by Wolfire et al. (2003).

These simulations represent two different scenarios: in the weak field case, the magnetic field has a turbulent component of the same order as its mean component. By contrast, in the strong field case, the magnetic field is mostly directed along the x-axis, that is, its projection is mainly contained in the xy and zx planes. The advantage of using simulations is that we can rotate each snapshot according to the three axes and calculate the quantities of interest integrated along three different LOSs, thus increasing our statistics. Table 2 summarises the ranges of the strength of the magnetic field in the plane perpendicular to a given LOS and their median values (marked by a superscript tilde) for the two snapshots under consideration. Specifically, for the LOS i, we compute the minimum and maximum values of the magnetic field strength, $B_{jk} = (B_j^2 + B_k^2)^{1/2}$, in the plane of the sky (POS) jk. Subscripts i, j, and k follow the cyclic permutation of Cartesian coordinates $(ijk) = \{xyz, yzx, zxy\}$.

4. Results

In contrast to typical angular resolutions of earlier facilities, such as the 5° of Guzmán et al. (2011), nowadays, LOFAR provides a significantly higher resolution, typically up to 4′ at frequencies of 115−189 MHz for observations of Galactic diffuse emission (Jelić et al. 2014, 2015; Van Eck et al. 2017). In the following, we show our results at the resolution of 6.7′. The latter value corresponds to the spatial resolution of the simulations (0.39 pc) if the simulation snapshots are placed at a distance of 200 pc. We focus on the frequency range 115−189 MHz, but the same conclusions apply to higher frequencies (see Sect. 5.2 and Appendix A).

4.1. Brightness temperature maps

Figure 5 shows the brightness temperature maps at a frequency $\nu = 130$ MHz for the two snapshots described in Sect. 3.2,

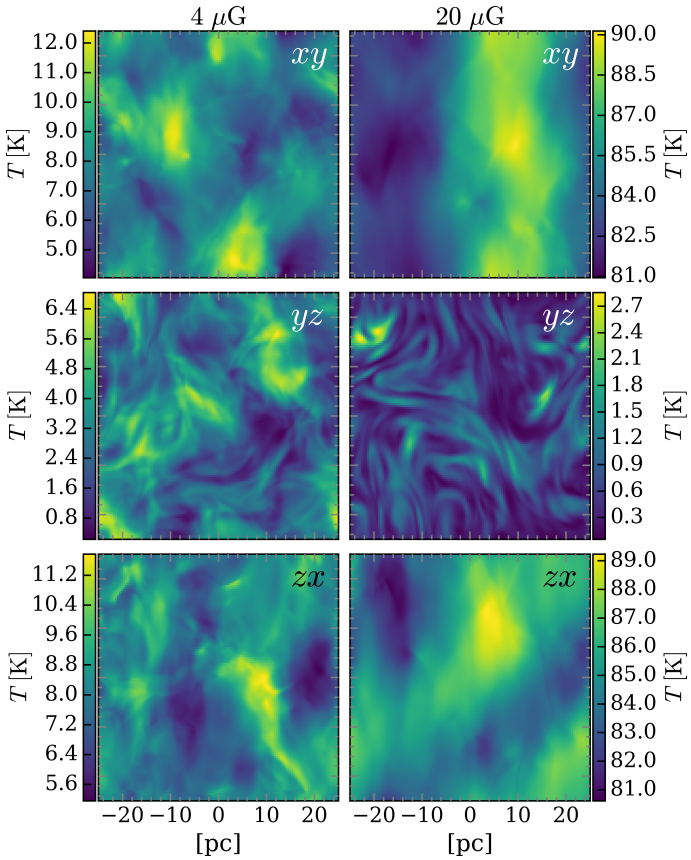

Fig. 5. Brightness temperature maps (colour scale) computed with the Orlando (2018) spectrum, at $\nu = 130$ MHz and with resolution 6.7′ for the three POSs (three rows, labelled xy, yz, and zx) of the weak and strong field cases (*left* and *right column*, respectively).

obtained with the CRe spectrum of Orlando (2018)[3]. These images are derived by integrating along the three different LOSs (x, y, z) over the length of the snapshot (50 pc), resulting in temperature maps identified by the respective POSs (yz, zx, xy). As anticipated by the upper panel of Fig. 4, the temperature is higher where $B_\perp$ is larger, reaching a maximum in the xy and zx POSs of the strong field case (right column of Fig. 5; see also the values of $\tilde{B}_{jk}$ in Table 2), while the smallest temperature values are in the yz POS of the strong field case. Temperature maps are more inhomogeneous in the yz POS of both snapshots. That is because, in these planes, $B_\perp$ has a significant turbulent component. Therefore, we introduce the ratio between the standard deviation and the median value of $B_\perp$, $\mu = \sigma_{B_\perp}/\tilde{B}_\perp$, to quantify the relative turbulent component of $B_\perp$. This quantity, the median values of which are reported in Table 3, is useful for the discussion on β and on the polarisation fraction in the following two sections.

4.2. Brightness temperature spectral index

We compute the brightness temperature spectral index, β, for each LOS, by a linear fit of $\log T_\nu$ versus $\log \nu$ for the three POSs of the two snapshots, in the frequency range 115–189 MHz with a frequency resolution of 183 kHz as in the LOFAR dataset by Jelić et al. (2015). In Fig. 6, we show the results in the form

[3] We verified that both the effect of synchrotron self-absorption (Ginzburg & Syrovatskii 1965) and the Tsytovich-Razin effect (Ginzburg & Syrovatskii 1964) can be neglected for the ISM under consideration.

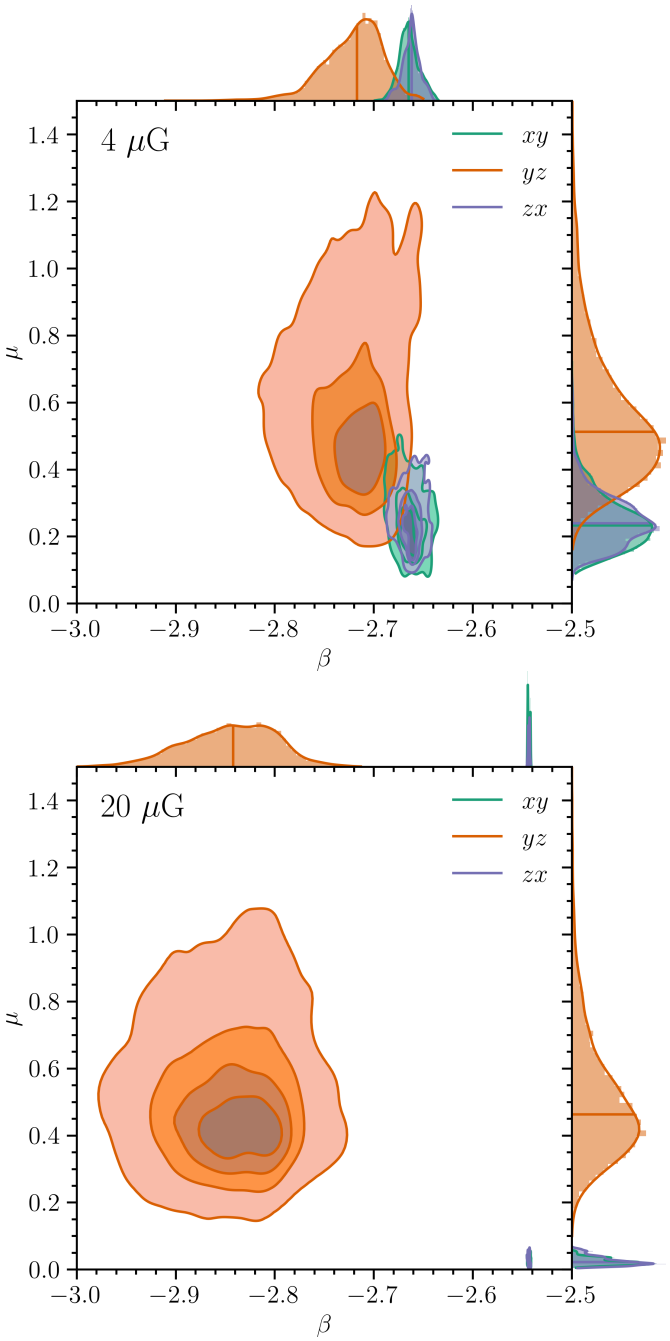

Fig. 6. Bivariate distribution of the ratio between the standard deviation of $B_\perp$ and its median value, μ, and the brightness temperature spectral index, β, computed in the frequency range 115−189 MHz for each LOS for the weak and strong field case (*upper* and *lower panel*, respectively), at a resolution of 6.7′. The POSs are identified by the three different colours displayed in the legend. Isodensity contours are plotted at 5, 30, 50, and 75% levels. The histograms above and to the right of the main plots show the marginal distribution of the two quantities. The median values are marked by horizontal and vertical lines and are listed in Table 3.

of bivariate and marginal distributions (see also Appendix B for the maps of β). From the inspection of Fig. 6, it is evident that in no case, at low frequencies, is β equal to −2.5, as would follow from the assumption of constant $s = -2$. As shown in Sect. 2.2, the same consideration holds in the high-frequency regime ($\nu \gtrsim 400$ MHz), where the assumption of constant $s = -3$,

Table 3. Medians of the ratio between the standard deviation of $B_\perp$ and its median value, $\mu = \sigma_{B_\perp}/\tilde{B}_\perp$, of the brightness temperature spectral index, and of the polarisation fraction at a resolution of 6.7′ for the three POSs and the two cases of weak and strong field[(a)].

	POS	$\tilde{\mu}$	$\tilde{\beta}$	$\tilde{p}$
Weak field ($B_0 = 4$ μG)	xy	$0.23^{+0.06}_{-0.05}$	-2.66 ± 0.01	$0.57^{+0.05}_{-0.06}$
	yz	$0.51^{+0.14}_{-0.10}$	-2.72 ± 0.02	0.34 ± 0.10
	zx	$0.24^{+0.05}_{-0.05}$	-2.66 ± 0.01	0.55 ± 0.06
Strong field ($B_0 = 20$ μG)	xy	0.02 ± 0.01	-2.54	0.70
	yz	$0.47^{+0.12}_{-0.09}$	-2.84 ± 0.03	$0.51^{+0.09}_{-0.13}$
	zx	0.02 ± 0.01	-2.54	0.70

Notes. [(a)]Errors have been estimated using the first and third quartiles. Errors smaller than 0.01 are not shown.

and hence $\beta = -3$, turns out to be incorrect. Figure 6 also shows that $\tilde{\beta}$ is less negative in the POSs xy and zx, where $\tilde{B}_\perp$ is larger (see also Tables 2 and 3). This is a consequence of what is shown in Fig. 3: for a given frequency, the larger the value of $B_\perp$ at a given position along the LOS, the smaller the median value of the energy range determining its synchrotron emissivity. Therefore, the corresponding values of s, and hence of β, increase. Finally, an important aspect to note is that the dispersion of β values around its median depends weakly on μ. Indeed, in both yz POSs, where μ reaches the largest values, the interquartile range (i.e. the difference between the third and the first quartile) is only 0.04 and 0.06 for the weak and the strong cases, respectively. For the sake of completeness, in Appendix A we show the bivariate distributions of μ and β for higher frequency ranges (467−672 MHz and 833−1200 MHz), which are used in Sect. 5.2. The conclusions are the same as for the 115−189 MHz range.

4.3. Polarisation fraction

The local polarisation fraction, that is, the polarisation fraction based on the local emissivities for an energy-independent value of s is

$$p = \frac{3 - 3s}{7 - 3s} = \frac{3 + 3\beta}{1 + 3\beta}, \tag{10}$$

(see, e.g. Rybicki & Lightman 1986), which, for $s = -2$ and -3, gives $p = 69$ and 75%, respectively. If the orientation and the strength of $\mathbf{B}_\perp$ do not vary along the LOS, Eq. (10) would also give the polarisation fraction in the POS. To quantify the limitations of the above assumption, we calculate the expected polarisation fraction (Eq. (8)) at the reference frequency $\nu = 130$ MHz for the two simulations and at the resolution of 6.7′ in the three POSs. Similarly to Fig. 6, in Fig. 7 we show the results in the form of bivariate and marginal distributions, and we find a similar correlation of μ with p as we found with β: as μ increases, the spread of values of p around its median value is even larger than that of β (see Table 3).

Furthermore, except for the POSs xy and zx in the strong field case, the median value is much lower than the theoretical value of ≃70% of the local polarisation fraction, which is the maximum value of the observed polarisation fraction. Such depolarisation effects in our study are mainly caused by the tangling of the turbulent component of the magnetic field along the LOS. This effect has been extensively reported in the literature in

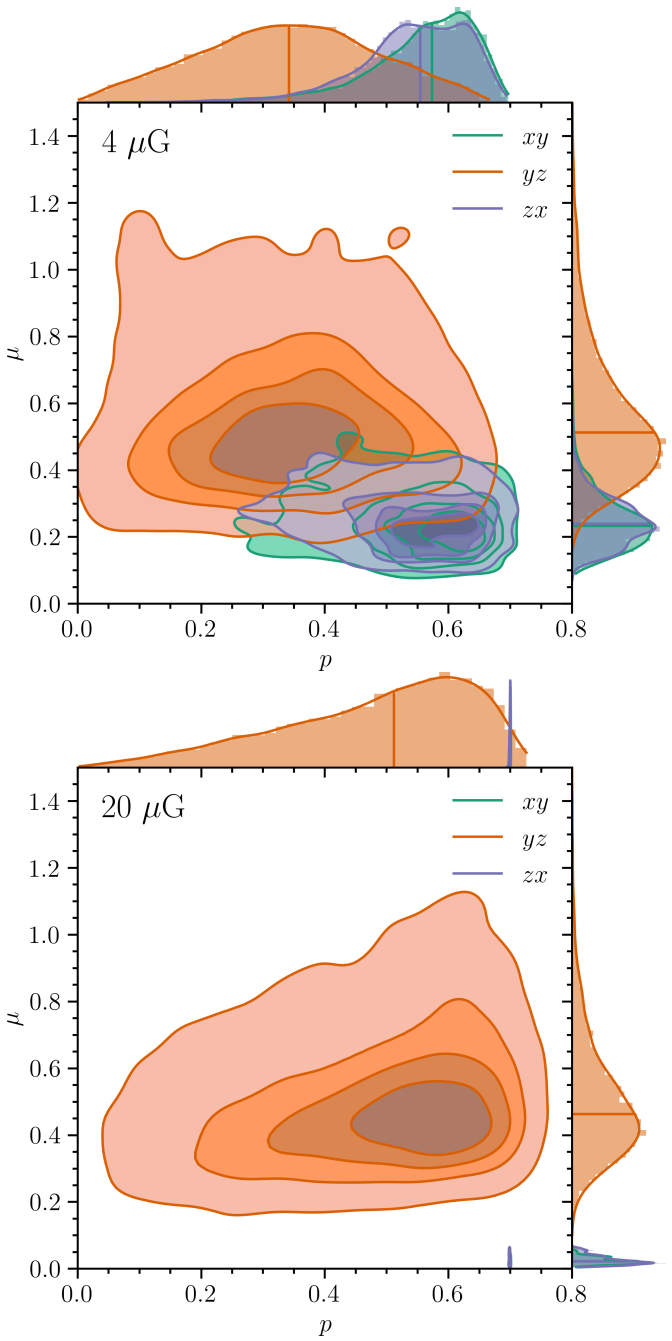

Fig. 7. Bivariate distribution of the ratio between the standard deviation of $B_\perp$ and its median value, μ, and the polarisation fraction, p, computed at 130 MHz for each LOS for the weak and strong field cases (*upper* and *lower panel*, respectively), at a resolution of 6.7′. The POSs are identified by the three different colours displayed in the legend. Isodensity contours are plotted at 5, 30, 50, and 75% levels. The histograms above and to the right of the main plots show the marginal distribution of the two quantities. The median values are marked by horizontal and vertical lines and are listed in Table 3.

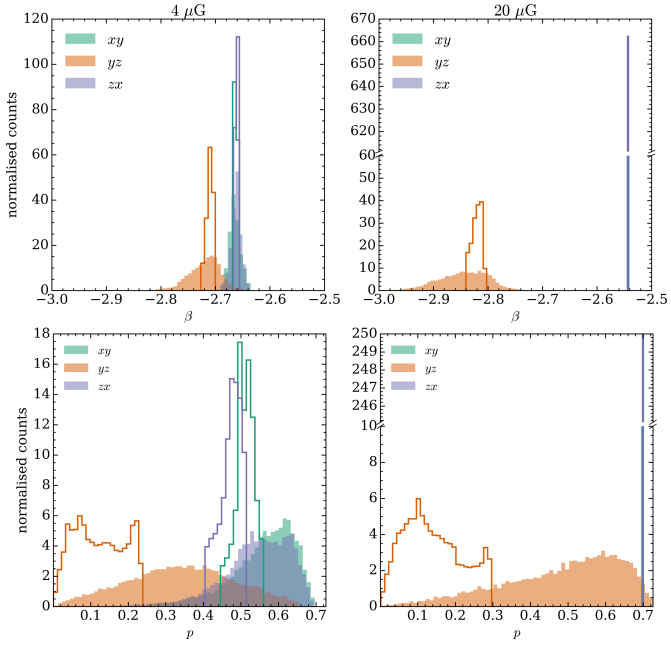

Fig. 8. Histograms of the spectral index β (*upper panels*) and polarisation fraction p (*lower panels*) for the weak and strong field cases (*left* and *right column*, respectively). Solid (empty) histograms refer to a resolution of 6.7′ (5°). The POSs are identified by the three different colours displayed in the legend.

both the radio (e.g. Gaensler et al. 2011) and in the submillimetre domains (e.g. Planck Collaboration Int XX 2015). Moreover, radio synchrotron polarisation can be severely affected by other mechanisms that drastically reduce the amount of detectable polarised emission, such as Faraday rotation and beam depolarisation (see, e.g. Sokoloff et al. 1998; Haverkorn et al. 2004). We note that Faraday rotation at a few hundred MHz cannot be neglected from an observational point of view. However, in this study we choose not to detail this process and to only focus on the emission mechanism of synchrotron radiation with an energy-dependent spectral slope. Faraday rotation will be the focus of a follow-up paper that will investigate the complexity of the ionisation degree of the multiphase diffuse ISM, a key ingredient to correctly model the effect of Faraday rotation.

5. Discussion

5.1. Effect of angular resolution on β and p

In this study we assumed the typical angular resolution of observations carried out with the most recent facilities, such as LOFAR. Here we show the distributions of the spectral index and the polarisation fraction obtained from lower resolution observations such as those shown in Guzmán et al. (2011). This latter paper presented an all-sky Galactic radio emission map, convolved to a common 5° resolution, combining observations obtained with different telescopes such as the Parkes 64 m, the Jodrell Bank MkI and MkIA, and the Effelsberg 100 m (Haslam et al. 1981, 1982), the Maipú Radio Astronomy Observatory 45-MHz array (Alvarez et al. 1997), and the Japanese Middle and Upper atmosphere radar array (MU radar; Maeda et al. 1999). Figure 8 shows the comparison of the distributions of β and p (upper and lower panels, respectively) at the resolutions of 6.7′ and 5° (filled and empty histograms, respectively). Despite the increase in resolution of LOFAR, the median value of β does not change appreciably (see upper panels). However, what does change is the spread of the distribution, because at a lower resolution it is not possible to pick up the finer variations of the spectral index. More interesting is how the polarisation fraction distributions differ in the two cases. The lower panels show the beam depolarisation effect mentioned in Sect. 4.3: where μ is larger, a lower resolution clearly results in a lower p.

5.2. A look-up plot for $B_\perp$

At any given position along a LOS, the synchrotron emission is jointly determined by the local CRe spectrum and the local value of $B_\perp$. As we show in Sect. 3.1, thanks to the range of β obtained from observations, it is possible to constrain the CRe spectrum at ~GeV energies (see also Fig. 3). This makes it possible to reduce the uncertainly on the spectral shape, an appreciable improvement over the assumption of an energy-independent s. One should also consider that the latest generation of telescopes, such as LOFAR and in the near future SKA, reach resolutions up to at least three orders of magnitude higher than previous instruments. This means that the uncertainties on the values of β derived from observations will be reduced and it will be possible to obtain β variations over smaller fields of view. Finally, in Sect. 4.2 we show that variations of $B_\perp$ along the LOS do not affect the estimates of β. This feature is particularly relevant for reducing the uncertainty in the estimation of the average value of $B_\perp$ along a LOS. Given these premises, we suggest a method for estimating $\langle B_\perp \rangle$, the average value of $B_\perp$, along a given LOS.

We adopt the Orlando (2018) CRe spectrum and assume ν in the range 10 MHz−20 GHz and $\langle B_\perp \rangle$ in the range 0.5−30 μG. We compute the corresponding emissivities (see Eqs. (1)) integrated along the LOS for 1 pc[4], and compute $\beta(\nu, \langle B_\perp \rangle) = \mathrm{d}\log T_\nu(\langle B_\perp \rangle)/\mathrm{d}\log\nu$. By inverting the relation for β, in Fig. 9 we show the values of $\langle B_\perp \rangle$ expected for each couple (ν, β).

We then consider three different ranges of frequencies: 115−189 MHz with a resolution of 183 kHz, 467−672 MHz with a resolution of 507 kHz, and 833−1200 MHz with a resolution of 908 kHz[5], labelled in Fig. 9 as low ($\mathcal{L}$), mid ($\mathcal{M}$), and high ($\mathcal{H}$) frequency range, respectively. Following the procedure described in Sect. 4.2, for each POS of the two snapshots, we calculate the temperature maps as a function of frequency at a resolution of 6.7′ and we extract the β value for each LOS and for each of the three frequency intervals, $\mathcal{L}$, $\mathcal{M}$, and $\mathcal{H}$, by a linear fit of $\log T_\nu$ versus $\log\nu$. We show in Fig. 9 the $\tilde{\beta}$ values for each POS by estimating the errors using the first and third quartiles for each frequency interval. We note that, as the POSs xy and zx for both snapshots have the same $\tilde{\beta}$, in the figure we show four values instead of six. The values of $\tilde{\beta}$ for the $\mathcal{L}$ frequency range are listed in Table 3, while those for the $\mathcal{M}$ and $\mathcal{H}$ ranges are reported in Table A.1.

Figure 9 shows that, for each POS, the estimates of $\tilde{\beta}$ in the three frequency intervals correspond to the same $\langle B_\perp \rangle$, which also agree with the respective value of $\tilde{B}_{jk}$ listed in Table 1. This confirms the consistency of our procedure.

This plot shows that there is a preferred range of frequencies that can be conveniently used to estimate $\langle B_\perp \rangle$ along a LOS. This range corresponds approximately to 100 MHz−5 GHz, the frequency interval where s, and hence β, varies the most and where the isocontours of $\langle B_\perp \rangle$ are more separated. Conversely, at frequencies that are too low (high), the CRe spectrum flattens out if $\langle B_\perp \rangle$ is too high (low), and the estimate of $\langle B_\perp \rangle$ becomes more uncertain. From this figure it can be concluded that, in order to have a more precise estimate of $\langle B_\perp \rangle$, it is advisable to simultaneously observe in narrow frequency ranges with high spectral resolution (as our $\mathcal{L}$, $\mathcal{M}$, and $\mathcal{H}$ intervals) in order to have independent β estimates that should follow a specific isocontour of $B_\perp$.

[4] As we are interested in β, results are independent of the LOS path length.

[5] Spectral resolutions were chosen so as to have the same number of frequency bins for the three frequency intervals considered.

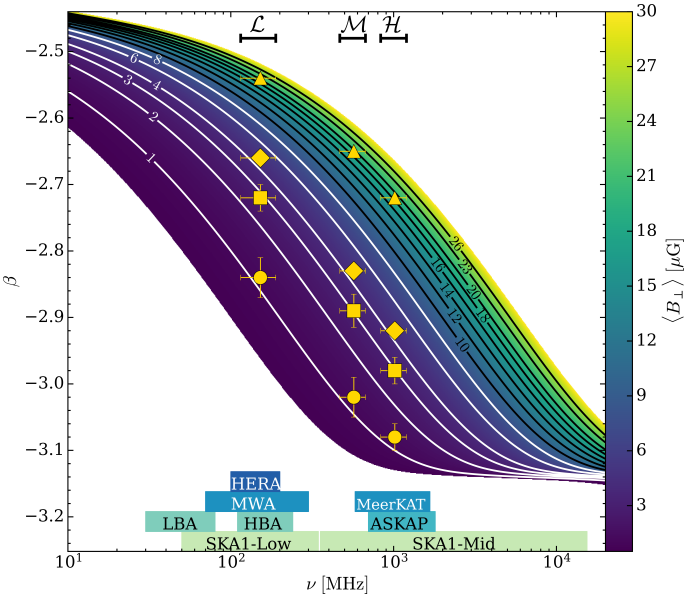

Fig. 9. Look-up plot with which to estimate the average value of $B_\perp$ along a LOS, $\langle B_\perp \rangle$, for a given frequency ν and brightness temperature spectral index β assuming the CRe spectrum by Orlando (2018). Black and white isocontours show specific values of $\langle B_\perp \rangle$ with labels in μG. Yellow symbols indicate estimates of $\langle B_\perp \rangle$ obtained from the values of $\tilde{\beta}$ in the frequency ranges 115−189 MHz, 467−672 MHz, and 833−1200 MHz (labelled as $\mathcal{L}$, $\mathcal{M}$, and $\mathcal{H}$, respectively) at a common resolution of 6.7′ for the different POSs of the two simulation snapshots (circles: POS yz in the strong field case; squares: POS yz in the weak field case; diamonds: POS xy and zx in the weak field case; triangles: POS xy and zx in the strong field case). Rectangles at the bottom of the plot show the frequency ranges of the low and high band antenna of LOFAR (LBA and HBA, respectively), the low and mid frequency bands of SKA (SKA1-Low and SKA1-Mid, respectively), and SKA pathfinders and precursors: the Hydrogen Epoch of Reionisation Array (HERA); the Murchison Widefield Array (MWA); the Karoo Array Telescope (MeerKAT); and the Australian SKA Pathfinder (ASKAP).

6. Summary

We carried out a quantitative study to understand the consequences of an energy-dependent CRe spectral slope for the interpretation of observations of synchrotron emission in the diffuse and magnetised ISM. We focused in particular on metre wavelengths that can currently be observed with state-of-the-art facilities such as LOFAR and in the near future with SKA. At frequencies lower (higher) than ≃400 MHz a constant spectral slope $s = -2$ ($s = -3$) is often assumed, mainly to avoid time-consuming calculations in analytical models and numerical simulations. As a consequence, one should also expect a constant value for the brightness temperature spectral index, β, related to s by $\beta = (s-3)/2$ (Rybicki & Lightman 1986). However, metre-wavelength observations show that β is not constant across the Galaxy, taking on values quite different from −2.5 (corresponding to $s = -2$), varying between about −2.7 and −2.1 (Guzmán et al. 2011).

For typical magnetic field strengths expected in the diffuse ISM (≃2−20 μG), the electrons that mostly determine the synchrotron emission at frequencies between about 100 MHz and 10 GHz have energies in the range ≃100 MeV−50 GeV. It is precisely at these energies that the spectral slope shows the largest variations. For example, for the CRe spectrum described in Orlando (2018), representative of intermediate Galactic latitudes

including most of the local emission within about 1 kpc around the Sun, in this energy range s varies between about −3.2 and −1.8.

In order to understand the effect of an energy-dependent spectral slope at a quantitative level, we first considered a slab with a fixed, spatially uniform $B_\perp$ exposed to a flux of CRe and we showed that, thanks to high-precision observational estimates of β at low frequencies (Mozdzen et al. 2017), it is possible to discard some realisations of the CRe spectrum that would imply unrealistically high values of $B_\perp$. We then used two snapshots of 3D MHD simulations (Bellomi et al. 2020) with different median magnetic field strength, and studied the synchrotron emission according to the CRe spectrum by Orlando (2018). We computed the distribution of β for three frequency ranges, at low, mid, and high frequencies (115−189 MHz, 467−672 MHz, and 833−1200 MHz, respectively). We show that the assumption of an energy-independent s is not justified and leads to non-negligible biases in the interpretation of the observed spectral index distributions. In particular, we find that β becomes less negative as $B_\perp$ increases and that the dispersion of the distribution of spectral index values around its median weakly depends on how much $B_\perp$ varies along the LOS. This property is of special relevance, because once a CRe spectrum is assumed, the uncertainty on the expected average value of $B_\perp$ for a given LOS, $\langle B_\perp \rangle$, is reduced. We then presented a look-up plot that makes it possible to estimate $\langle B_\perp \rangle$ given β values obtained from observations in one or more frequency intervals. More precisely, we suggest repeating observations in narrow frequency intervals with high spectral resolution in order to have independent estimates of β that should lie on the same $\langle B_\perp \rangle$ isocontour in the look-up plot.

Finally, we computed the expected polarisation fraction, p, finding that it is expected to decrease as the turbulence of the magnetic field along the LOS increases, deviating noticeably from the maximum value of ≃70%. The dispersion of p around its median value is larger than that of β as a consequence of the turbulent tangling of the magnetic field lines along the LOS. The analysis of this depolarisation effect and the consequences of Faraday rotation are deferred to a subsequent paper.

Acknowledgements. The authors wish to thank the referee, Katia Ferrière, for her careful reading of the manuscript and insightful comments that considerably helped to improve the paper. M.P. thanks Tommaso Grassi for useful discussions. A.B. acknowledges the support from the European Union's Horizon 2020 research and innovation program under the Marie Skłodowska-Curie Grant agreement No. 843008 (MUSICA). V.J. acknowledges support by the Croatian Science Foundation for the project IP-2018-01-2889 (LowFreqCRO).

References

Ackermann, M., Ajello, M., Atwood, W. B., et al. 2010, Phys. Rev. D, 82, 092004
Adriani, O., Barbarino, G. C., Bazilevskaya, G. A., et al. 2011, Phys. Rev. Lett., 106, 201101
Aguilar, M., Aisa, D., Alvino, A., et al. 2014, Phys. Rev. Lett., 113, 121102
Alvarez, H., Aparici, J., May, J., & Olmos, F. 1997, A&AS, 124, 205
Beck, R. 2015, A&ARv, 24, 4
Bellomi, E., Godard, B., Hennebelle, P., et al. 2020, A&A, 643, A36
Berger, M. J., & Oliger, J. 1984, J. Comput. Phys., 53, 484
Bowman, J. D., Rogers, A. E. E., Monsalve, R. A., Mozdzen, T. J., & Mahesh, N. 2018, Nature, 555, 67
Bracco, A., Jelić, V., Marchal, A., et al. 2020, A&A, 644, L3
Chapman, E., & Jelić, V. 2019, in The Cosmic 21-cm Revolution, (Bristol: IOP Publishing), 2514, 6
Cummings, A. C., Stone, E. C., Heikkila, B. C., et al. 2016, ApJ, 831, 18
Dewdney, P. E., Hall, P. J., Schilizzi, R. T., & Lazio, T. J. L. W. 2009, IEEE Proc., 97, 1482
Federrath, C., Roman-Duval, J., Klessen, R. S., Schmidt, W., & Mac Low, M.-M. 2010, A&A, 512, A81
Ferrière, K. 2020, Plasma Phys. Controll. Fusion, 62, 014014
Field, G. B. 1965, ApJ, 142, 531
Field, G. B., Goldsmith, D. W., & Habing, H. J. 1969, ApJ, 155, L149
Fromang, S., Hennebelle, P., & Teyssier, R. 2006, A&A, 457, 371
Gaensler, B. M., Haverkorn, M., Burkhart, B., et al. 2011, Nature, 478, 214
Gehlot, B. K., Mertens, F. G., Koopmans, L. V. E., et al. 2019, MNRAS, 488, 4271
Ginzburg, V. L., & Syrovatskii, S. I. 1964, The Origin of Cosmic Rays (London: Pergamon Press)
Ginzburg, V. L., & Syrovatskii, S. I. 1965, ARA&A, 3, 297
Grenier, I. A., Black, J. H., & Strong, A. W. 2015, ARA&A, 53, 199
Guzmán, A. E., May, J., Alvarez, H., & Maeda, K. 2011, A&A, 525, A138
Habing, H. J. 1968, Bull. Astron. Inst. Netherlands, 19, 421
Haslam, C. G. T., Klein, U., Salter, C. J., et al. 1981, A&A, 100, 209
Haslam, C. G. T., Salter, C. J., Stoffel, H., & Wilson, W. E. 1982, A&AS, 47, 1
Haverkorn, M., Katgert, P., & de Bruyn, A. G. 2004, A&A, 427, 549
Heiles, C., & Troland, T. H. 2003a, ApJ, 586, 1067
Heiles, C., & Troland, T. H. 2003b, VizieR Online Data Catalog: II/145
Heiles, C., & Troland, T. H. 2005, ApJ, 624, 773
Ivlev, A. V., Padovani, M., Galli, D., & Caselli, P. 2015, ApJ, 812, 135
Jelić, V., de Bruyn, A. G., Mevius, M., et al. 2014, A&A, 568, A101
Jelić, V., de Bruyn, A. G., Pandey, V. N., et al. 2015, A&A, 583, A137
Kalberla, P. M. W., & Haud, U. 2018, A&A, 619, A58
Khokhlov, A. M. 1998, J. Comput. Phys., 143, 519
Longair, M. S. 2011, High Energy Astrophysics (Cambridge: Cambridge University Press)
Maeda, K., Alvarez, H., Aparici, J., May, J., & Reich, P. 1999, A&AS, 140, 145
Marchal, A., Miville-Deschênes, M.-A., Orieux, F., et al. 2019, A&A, 626, A101
Mertens, F. G., Mevius, M., Koopmans, L. V. E., et al. 2020, MNRAS, 493, 1662
Mozdzen, T. J., Bowman, J. D., Monsalve, R. A., & Rogers, A. E. E. 2017, MNRAS, 464, 4995
Mozdzen, T. J., Mahesh, N., Monsalve, R. A., Rogers, A. E. E., & Bowman, J. D. 2019, MNRAS, 483, 4411
Murray, C. E., Stanimirović, S., Goss, W. M., et al. 2015, ApJ, 804, 89
Murray, C. E., Stanimirović, S., Goss, W. M., et al. 2018, ApJS, 238, 14
Orlando, E. 2018, MNRAS, 475, 2724
Padovani, M., Galli, D., & Glassgold, A. E. 2009, A&A, 501, 619
Padovani, M., Ivlev, A. V., Galli, D., & Caselli, P. 2018, A&A, 614, A111
Planck Collaboration IV. 2020, A&A, 641, A4
Planck Collaboration Int. XX. 2015, A&A, 576, A105
Platania, P., Bensadoun, M., Bersanelli, M., et al. 1998, ApJ, 505, 473
Reich, P., & Reich, W. 1988a, A&AS, 74, 7
Reich, P., & Reich, W. 1988b, A&A, 196, 211
Reissl, S., Brauer, R., Klessen, R. S., & Pellegrini, E. W. 2019, ApJ, 885, 15
Roger, R. S., Costain, C. H., Landecker, T. L., & Swerdlyk, C. M. 1999, A&AS, 137, 7
Rybicki, G. B., & Lightman, A. P. 1986, Radiative Processes in Astrophysics (Hoboken: Wiley), 400
Schmidt, W., Federrath, C., Hupp, M., Kern, S., & Niemeyer, J. C. 2009, A&A, 494, 127
Sokoloff, D. D., Bykov, A. A., Shukurov, A., et al. 1998, MNRAS, 299, 189
Stone, E. C., Cummings, A. C., Heikkila, B. C., & Lal, N. 2019, Nat. Astron., 3, 1013
Strong, A. W., Moskalenko, I. V., & Ptuskin, V. S. 2007, Ann. Rev. Nucl. Part. Sci., 57, 285
Sun, X. H., Reich, W., Waelkens, A., & Enßlin, T. A. 2008, A&A, 477, 573
Teyssier, R. 2002, A&A, 385, 337
Trott, C. M., Jordan, C. H., Midgley, S., et al. 2020, MNRAS, 493, 4711
van Haarlem, M. P., Wise, M. W., Gunst, A. W., et al. 2013, A&A, 556, A2
Van Eck, C. L., Haverkorn, M., Alves, M. I. R., et al. 2017, A&A, 597, A98
Waelkens, A., Jaffe, T., Reinecke, M., Kitaura, F. S., & Enßlin, T. A. 2009, A&A, 495, 697
Wang, J., Jaffe, T. R., Enßlin, T. A., et al. 2020, ApJS, 247, 18
Wolfire, M. G., McKee, C. F., Hollenbach, D., & Tielens, A. G. G. M. 2003, ApJ, 587, 278

Appendix A: Bivariate distributions of μ and β at high frequencies

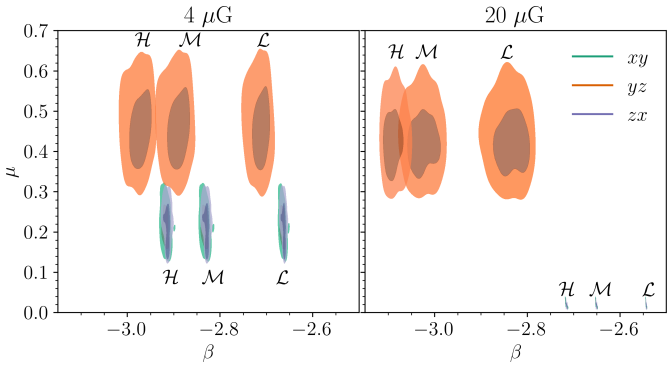

Fig. A.1. Bivariate distribution of the ratio between the standard deviation of $B_\perp$ and its median value, μ, and the brightness temperature spectral index, β, computed in the frequency ranges 115−189 MHz, 467−672 MHz, and 833−1200 MHz (labelled $\mathcal{L}$, $\mathcal{M}$, and $\mathcal{H}$, respectively) for each LOS for the weak and strong field case (*left* and *right panel*, respectively), at a resolution of 6.7′. The POSs are identified by the three different colours displayed in the legend. Isodensity contours are plotted at 50 and 80%.

Table A.1. Medians of the brightness temperature spectral index for the three POSs and the two cases of weak and strong field at a resolution of 6.7′.

	POS	$\tilde{\beta}$	
		$\mathcal{M}$	$\mathcal{H}$
Weak field ($B_0 = 4$ μG)	xy	-2.83 ± 0.01	-2.92 ± 0.01
	yz	-2.89 ± 0.02	-2.98 ± 0.02
	zx	-2.83 ± 0.01	-2.92 ± 0.01
Strong field ($B_0 = 20$ μG)	xy	-2.65	-2.72
	yz	-3.02 ± 0.03	-3.08 ± 0.02
	zx	-2.65	-2.72

Notes. Labels $\mathcal{M}$ and $\mathcal{H}$ identify the frequency intervals 467−672 MHz and 833−1200 MHz, respectively. Errors have been estimated using the first and third quartiles. Errors smaller than 0.01 are not shown.

Following the procedure outlined in Sect. 4.2, we consider two higher frequency ranges, 467−672 MHz and 833−1200 MHz (labelled $\mathcal{M}$ and $\mathcal{H}$, respectively), for the calculation of β in the three POSs of the two simulation snapshots. Figure A.1 shows the bivariate distribution of μ and β for these two frequency ranges, comparing them with the distribution for the range 115−189 MHz (labelled $\mathcal{L}$) described in Sect. 4.2. In order to increase clarity and to avoid overlapping distributions, we only show isodensity contours plotted at 50 and 80%. As the frequency range increases, the β distributions shift towards more negative values. This can be explained by looking at Fig. 3 where we see that as the frequency increases, the energies determining the synchrotron emissivity are higher and higher. Higher energies correspond to more negative values of s, and therefore of β. For completeness, Table A.1 shows the values of $\tilde{\beta}$ for the three POSs of the two snapshots considered in the frequency intervals $\mathcal{M}$ and $\mathcal{H}$.

Appendix B: Brightness temperature spectral index maps

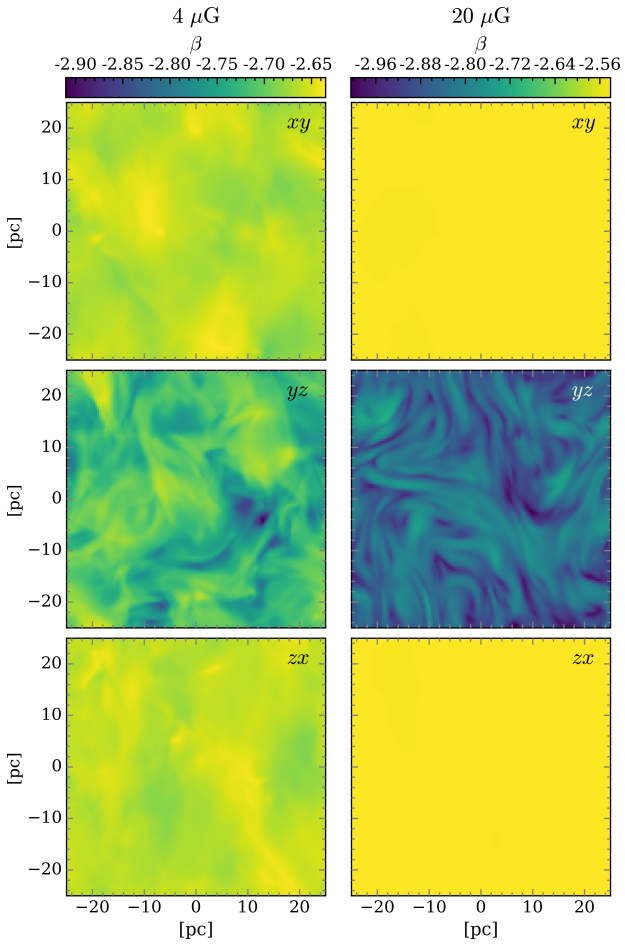

Fig. B.1. Brightness temperature spectral index maps for the three POSs (*three rows*) of the weak and strong field case (*left and right column*, respectively) for a resolution of 6.7′. The *three panels* of each column share the same colour bar at the *top*.

Here we show the spectral index maps obtained for the two simulations described in Sect. 3.2. These maps have been derived considering the same frequency range and frequency resolution of LOFAR observations by Jelić et al. (2015), namely $\nu = 115-189$ MHz and $\Delta\nu = 183$ kHz, respectively. In the POS where $\mu \ll 1$, namely the xy and zx POSs of the strong field case, β shows a constant value. Moreover, the greater the turbulent component of the field, the greater the variations exhibited by β on small scales. The latter can in principle be resolved by observations with LOFAR. From these maps, the histograms displayed in Fig. 6 were produced.